Impact of Activation Energy and Heat Source/Sink on 3D Flow of Williamson Nanofluid with Gan Nanoparticles over A Stretching Sheet

Mamidala Jyotshna and Vadlakonda Dhanalaxmi

***Abstract* — Several novel techniques for the study of thermophysical characteristics have opened up new avenues for understanding the flow and heat transfer effects in nanofluids, leading to novel applications. There have been studies on nanofluids including different metal, ceramic and magnetic nanoparticles mixed with base fluids such as Water, Kerosene, and Ethylene glycol. However, research using semiconductor nanoparticles is restricted. For the investigation, Gallium nitrite, a binary semiconductor with excellent heat convection combined with base fluid Ethylene glycol in nanoparticle form, is employed. Williamson MHD nanofluid (GaN nanoparticles + Ethylene glycol) is examined across a stretched sheet with porosity under the impact of convective boundary conditions, thermal radiation, thermal source/sink, and activation energy in three dimensions. The governing equations are turned into dimensionless ordinary differential equations via similarity transformations. Numerical analysis was carried out in MATLAB utilizing bvp5c and the shooting technique. The results are visually shown, and plausible scientific explanations for the velocity, temperature, and concentration profiles with respect to different parameters are provided. In addition, the Skin-friction coefficient, Nusselt number, and Sherwood number are presented in tabular form. The velocity and temperature profiles increased while the concentration profile decreased as the volume fraction of Gallium nitride nanoparticles in the Williamson nanofluid increased. Physical significances were also assigned to each observed outcome.**

***Keywords* — Activation energy, Gallium nitride, heat source/sink, volume fraction, Williamson nanofluid.**

I. Introduction

Heat transport study in fluids has been an important issue for the technical workforce in the industry and through them a challenge to increase the surface area of heat exchange. Industrialists face this problem due to the poor convective properties of the fluids used for the purpose. Therefore, an essential demand was created to improve the capacity of thermal conductivity of the conventional fluids or to search for new methods and fluids which improve the heat exchange process. Attention was also drawn towards Maxwell, Casson, Power law, and Williamson types of fluids. Williamson fluid is a non-Newtonian fluid with low viscosity at a high rate of shear stress i.e., the effective viscosity of Williamson fluid should drop independently as shear rate increases, which means, the fluid possesses infinite viscosity under no stress situation and nil viscosity as shear rate approaches infinity. Navier stroke equations do not adequately represent non-Newtonian fluids. Because of the flexible character of these fluids, constitutive equations will contain numerous rheological components, making them more difficult than equations describing viscous fluid movement. As a result, several non-Newtonian fluid models have been introduced in the literature. Such fluids also possess many industrial applications such as lubrication, rotating machinery, and viscometry. Reference [1] investigated MHD three-dimensional layer flow of Williamson fluid restricted by bidirectional stretched surface and concluded that when the stretching ratio parameter grows, velocity along the x-axis increases while velocity along the y-axis decreases. Reference [2] examined the thermal properties of Casson nanofluids in Darcy porous media. Reference [3] explained suspension studies on single-walled carbon nanotubes and multiwalled carbon nanotubes due to a flat plate while considering boundary conditions and concluded the effect of volume fraction of nanoparticles in fluid, Prandtl number, and heat transfer, which resulted in various applications in science and engineering applications. As the research progresses, boomingly, nanofluids are identified as better fluids over conventional fluids. Reference [4] gave an indication and explained the possibilities to obtain better heat transfer in nanofluids. In their work, [5] discussed the analysis and technique of synthesizing several nanofluids by directly

Published on September 5, 2022.
M. Jyotshna Department of Mathematics, Maturi Venkata Subba Rao Engineering College, Osmania University, India.
(corresponding e-mail: mamidala.jyotsna@gmail.com)
V. Dhanalaxmi University College of Technology, Osmania University, India.

combining nanophase powders with base fluids. The current and future applications of nanofluids were revealed by [6] Nanofluids, are now considered a modern class of fluids, which consists of nanoparticles mixed with base fluids like water, ethylene glycol, propylene glycol, oil and possess better thermal conductivity than base fluids. Reference [7] created the term nanofluids for the first time in 1995 and proposed that nanofluids may be classified as a new class of fluids used to enhance heat transfer mechanisms due to possible thermo-physical characteristics of nanoparticles in specified base fluids. Williamson nanofluid is also one such fluid that can replace conventional fluids [8]–[11]. Nanofluids are utilized in a wide range of industrial applications due to their distinguishing characteristics, such as coolants in heat exchangers, radiators, nuclear reactors, solar collectors, thermal reading across a flat surface, radiators, microelectronic devices, and so on. Applications of nanofluids are also in the medical field such as disease diagnosis, drug delivery, wound dressing, etc. Later, numerous researchers and scientists expanded on this notion to achieve spectacular results in flow and heat transmission [12]-[15]. All these investigations found that nanofluids were unable to offer the high heat transfer rates necessary for large-scale businesses. To compensate for this weakness, hybrid nanofluids are formed by mixing one or more distinct nanoparticles in a carrier fluid [16]. When compared to carrier fluids and nanofluids, these hybrid nanofluids will have better thermal properties. Reference [17] have investigated the flowing behavior of a hybrid nanofluid across a rotating disc in presence of activation energy [16]. Reference [18] investigated the heat transfer mechanism and flow of a propylene glycol-water based fluid with hybrid nanoparticle suspension [16].

Nanofluid flow over a stretched sheet with heat transfer is crucial in terms of engineering and design applications. We can specifically pinpoint its uses: cooling of a metallic shield, plastic sheet extrusion, glass fiber production, wire drawing, polymer extrusion process, cooling shower, metal turning process, and so forth. Reference [19] have investigated the flow of fluids past a stretched sheet. References [20] and [21] investigated MHD nanofluid flow over a non-linear stretching sheet and studied the effect of viscous dissipation on the flow of a magnetized nanofluid on a curved stretching sheet [16]. Reference [22] described a mixed convective stream of fluid with carbon nanotubes flowing across an arched stretched sheet under the influence of a magnetic field [16]. 3D Williamson fluid flow over a stretching sheet has been surveyed by [23] and [24]. Three-dimensional nanofluid flow under various conditions like thermal radiation over a non-linear stretching sheet with slip [25] and [26], electromagnetic radiative non-Newtonian flow with Joule heating associated with chemical reaction in porous materials [27], hydro-magnetic convective and chemically reactive Williamson nanofluid with non-uniform heat absorption and generation [28], the effect of variable thermal conductivity on nanofluid flow over a stretching sheet [29] were addressed and explained in terms of thermal diffusion of nanofluid. Three-dimensional nanofluid stirring with a non-uniform heat source / sink through an elongated sheet was studied by [30] and observed that increasing the stretching ratio parameter affects the axial velocity profile, whereas cooling of the sheet affects the transverse velocity. Reference [31] analyzed the thermal conductivity of the H_2O-titania nanofluid Vs particle concentration and temperature using an Artificial Neural Network (ANN) and Response Surface Methodology (RSM) and determined that the neural network comprises two hidden layers with 2 and 4 neurons. Reference [32] stretched the surface to examine stratified mixed convection thixotropic nanofluids flow. Reference [33] investigated MHD viscoelastic nano liquid flow in the presence of nonlinear radiation. References [34]–[36] discussed the mixed convective flow of a viscous liquid with a chemical reaction between two revolving discs. The flow of a third-grade liquid across an exponentially stretched surface with chemical reaction and magnetohydrodynamics was thoroughly investigated. Reference [37] use the Homotopy approach for analytical solutions of three-dimensional MHD flow over a linearly stretching sheet in the presence of nanoparticles and nonlinear thermal radiation. Reference [38] investigated the impact of nanoparticles on three-dimensional MHD flow across a bidirectionally expanding sheet. Reference [39] statistically investigated the topic of nanofluid stagnation point flow. They investigated water-based nanofluids with three distinct types of nanoparticles: copper (Cu), alumina (Al_2O_3), and Titania (TiO_2). All of the works described above dealt with linear stretching sheet difficulties. The stretching sheet is not always linear in many practical situations. Reference [40] investigated three-dimensional boundary layer flow caused by a non-linear stretching sheet. Reference [41] conducted numerical simulation studies on the beat transfer performance of ZrO_2-water Cu-water nanofluids in a tube with a concentric double twisted element (CDTE) and discovered that the Nusselt numbers of Cu-water nanofluid were higher than those of ZrO_2-water nanofluid.

The thermal behavior of base fluid Ethylene Glycol added with ferromagnetic nanoparticles like Fe2O4, $NiZnFe_2O_4$, and $MnZnFe_2O_4$ on the stretching sheet was studied by [42] under boundary conditions and compared the effects of magnetic dipole interactions on the fluid flow. The impacts of emerging parameters on the magneto-thermomechanical coupling were analyzed by them numerically. Reference [43] discussed the flow of nanofluids consisting of $NiZnFe_2O_4$ nanoparticles and ethylene glycol over a curved surface to understand the heat transfer flow and concluded that the Schmidt and Prandtl numbers lower the fluid concentration. Reference [44] studied the thermophysical characteristics and heat transport properties of an

exceptionally stable $CoFe_2O_4$/GO nanofluid generated in green. Reference [45] investigated the properties of a fraction model of MHD flow of Casson fluid including cadmium telluride nanostructures using the extended Fourie's law.

Summarily, the researchers have studied the flow of nanofluids consisting of metallic (Cu, Ag, Au), nonmetallic (MgO, TiO_2, Al_2O_3), ferrite (Fe_2O_3, $ZnFe_2O_3$, $CoFe_2O_3$) nanoparticles [46]–[51] under various conditions like stretching sheet, inclined magnetic field, thermal flux, nonlinearly stretched porous sheet, etc. Water, transformer oil, ethylene glycol, and toluene have so far been identified as base fluids. Various nanoparticles studied till now, may broadly be classified into three types: pure metallic nanoparticles, ceramic nanoparticles, and carbon nanotubes (CNTs). The distinct combination of the particles mentioned above and different fluids result in various nanofluids. In this study, nanofluids are classified mostly by the type of nanoparticles used for realizing their respective nanofluids. The study of nanofluids consisting of semiconductor compound nanoparticles (SCNPs) is not studied except in a few papers published on ZnO [52], [53], and CdTe [45] semiconductor nanoparticles. Some semiconductor compounds with a high melting point (> 1000 °C) may not cause deviation in bond strengths ensuring no deviation from its density parameters. At the same time, these nanoparticles have good thermal properties like the convection of heat. Therefore, it is felt that the results on heat transfer of nanofluids consisting of SCNPs under different external force and boundary conditions are interesting and may have industrial applications. Hence, the present analysis attempts the study of Williamson fluid consisting of GaN nanoparticles and base fluid, Ethylene glycol running over a linearly stretched porous sheet under the influence of the magnetic field, hear source/sink, radiation, Arrhenius activation energy to understand temperature, velocity, and concentration profiles. GaN semiconductor compound nanoparticles, nowadays, are intensely used in the preparation of photo sensors, solar cells, and prominent electronic industries due to their outstanding mechanical, physical, and chemical properties resulting from size effects [54]–[56]. Investigations on nanofluids consisting of GaN nanoparticles are not attempted till now therefore, the present studies are initiated.

II. Mathematical Model

A. The Governing Equations

To establish a mathematical model for a 3-dimensional boundary layer flow, a liquid flow under steady-state, laminar, incompressible viscous nanofluid past a stretching sheet is considered under the following assumptions.

- The sheet is stretched laterally along x and y -axes with the velocity $u_w(x) = ax$, and $v_w(y) = by$ (a,b are stretching constants) respectively. Fig. 1 shows the physical representation of the problem.
- The sheet has a uniform surface temperature (T_w) and concentration (C_w) coinciding with the plane z=0, where the z-axis is perpendicular to the movement of the fluid with the flow confined to a half-plane of $z > 0$.
- T_∞ and C_∞ represent ambient fluid temperature and concentration respectively (at its free surface).
- Williamson nanofluid flow consists of GaN nanoparticles of uniform shape and size and base fluid of ethylene glycol.
- The magnetic field of uniform field strength B_o is applied normal to the stretched surface (kept in the XY plane) i.e., along Z-direction.
- Reynolds number of the fluid is considered to be small, therefore, the induced magnetic field in the fluid is neglected.
- The pressure gradient along the linear stretched sheet is negligible $\partial p/\partial x = 0$).

The heat transport mechanism in Williamson nanofluid at par linearly stretched porous sheet applied with uniform magnetic field in presence of non-linear thermal radiation and activation energy is carried out. The thermophysical properties of nanoparticles and the base fluid considered in the present investigation are given in Table I.

The model of Williamson fluid is taken [28], [57], [58] as

$$\dot{S} = -\dot{p}I + \tau \tag{1}$$

$$\tau = [\mu_\infty + \frac{(\mu_0 - \mu_\infty)}{1-\Gamma\dot{\gamma}}]A_1, \tag{2}$$

The symbols in the above equations represent τ - extra stress tensor; S - Cauchy stress tensor; I - identity vector; p- pressure; μ_0 −limiting viscosity at zero shear rate; A_1 - first Rivlin- Erickson tensor; μ_∞- limiting viscosity at infinity shear rate; $\Gamma > 0$ - time constant;

$$\dot{\gamma} = \sqrt{\{\frac{1}{2} trace\ (A_1^2)\}}, \tag{3}$$

Here, they are all measured in the case of $\mu_\infty = 0$ and $\Gamma\dot{\gamma} < 1$.

Thus, τ takes the form $\tau = [\ \frac{\mu_0}{1-\Gamma\dot{\gamma}}]A_1$ (4)

Applying binomial expansion to (4), we get

$$\tau = \mu_0[\ 1 + \Gamma\dot{\gamma}]A_1. \quad (5)$$

The governing equations and the associated boundary conditions [1], [15], [28], [59], [60] are as follows

$$\frac{\partial u}{\partial x} + \frac{\partial v}{\partial y} + \frac{\partial w}{\partial z} = 0 \quad (6)$$

$$\mathrm{u}\ \frac{\partial u}{\partial x} + v\frac{\partial u}{\partial y} + w\frac{\partial u}{\partial z} = \frac{\mu_{nf}}{\rho_{nf}}\frac{\partial^2 u}{\partial y^2} + \sqrt{2}\frac{\mu_{nf}}{\rho_{nf}}\Gamma\frac{\partial u}{\partial z}\frac{\partial^2 u}{\partial z^2} - \frac{\sigma {B_o}^2}{\rho_{nf}}u - \frac{\mu_{nf}}{\rho_{nf}K_p}u \quad (7)$$

$$\frac{\partial v}{\partial x} + v\frac{\partial v}{\partial y} + w\frac{\partial v}{\partial z} = \frac{\mu_{nf}}{\rho_{nf}}\frac{\partial^2 v}{\partial y^2} + \sqrt{2}\frac{\mu_{nf}}{\rho_{nf}}\Gamma\frac{\partial v}{\partial z}\frac{\partial^2 v}{\partial z^2} - \frac{\sigma {B_o}^2}{\rho_{nf}}v - \frac{\mu_{nf}}{\rho_{nf}K_p}v \quad (8)$$

$$\mathrm{u}\ \frac{\partial T}{\partial x} + v\frac{\partial T}{\partial y} + w\frac{\partial T}{\partial z} = \alpha_{nf}\ \frac{\partial^2 T}{\partial y^2} - \frac{1}{(\rho c_p)_{nf}}\frac{\partial q_r}{\partial z} + \frac{Q_o(T-T_\infty)}{(\rho c_p)_{nf}} \quad (9)$$

$$u\ \frac{\partial C}{\partial x} + v\frac{\partial C}{\partial y} + w\frac{\partial C}{\partial z} = D_B\ \frac{\partial^2 C}{\partial y^2} - K_o^2(c - c_\infty)\left(\frac{T}{T_\infty}\right)^m \exp\left(\frac{-E_a}{kT}\right) \quad (10)$$

By Rosseland approximation, the radiative heat flu $\frac{\partial q_r}{\partial z}$ [27] is given by $\frac{\partial q_r}{\partial z} = \frac{16\,\sigma^* T_\infty^3}{3\,k^*}\frac{\partial^2 T}{\partial z^2}$

B. *Boundary Conditions*

According to [28] the boundary conditions for the velocity, temperature, and concentration fields are:

$$z = 0: \qquad u = u_w, \qquad v = v_w, \qquad w = 0, \ -K\frac{\partial T}{\partial z} = h_f(T_w - T), \qquad C \to C_w$$

$$z \to \infty: \qquad u \to 0, \qquad v \to 0, \qquad T \to \mathrm{T}_\infty \qquad C \to C_\infty \quad (11)$$

where h_f represents the heat transfer coefficient and K the thermal conductivity.

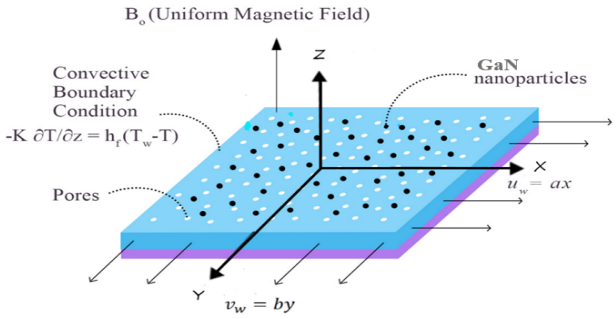

Fig. 1. Diagrammatic representation of the problem.

TABLE I: THERMO-PHYSICAL PROPERTIES OF THE FLUID AND NANOPARTICLES

Physical parameters	Ethylene glycol($C_2H_6O_2$) [61]	Gallium nitride (GaN) [62], [63]
ρ (kg/m^3)	1115	6150
Cp (J/kgK)	2430	431
k (W/mK)	0.253	230

The mathematical expressions for different thermo-physical properties of nanofluid are given below in Table II.

TABLE II: MATHEMATICAL EQUATIONS OF THERMOPHYSICAL PROPERTIES OF NANOFLUID [46], [64]

Properties	Equation(s)
Thermal Diffusivity	$\alpha_{nf} = \frac{k_{nf}}{(\rho c_p)_{nf}}$
Dynamic Viscosity	$\mu_{nf} = \frac{\mu_f}{(1-\Phi)^{2.5}}$
Thermal conductivity	$K_{nf} = K_f\left(\frac{K_s + 2K_f - 2\Phi(K_f - K_s)}{K_s + 2K_f + \Phi(K_f - K_s)}\right)$
Density	$\rho_{nf} = (1-\Phi)\rho_f + \Phi\rho_s$
Heat capacity	$(\rho C_p)_{nf} = (1-\Phi)(\rho C_p)_f + \Phi(\rho C_p)_s$
Kinematic viscosity	$\nu_f = \frac{\mu_f}{\rho_f}$

C. Similarity Equations

The similarity equations are used to transform the governing (7) to (10) into a set of ordinary differential equations by considering the three-dimensional linear similarity transformations

$$u = axf'(\eta), \qquad v = ayg'(\eta), \qquad w = -\sqrt{pv_f}(f(\eta)+g(\eta))$$
$$\theta(\eta) = \frac{T-T_\infty}{T_w-T_\infty}, \qquad \eta = z\sqrt{a/v_f}, \qquad \emptyset(\eta) = \frac{C-C_\infty}{C_w-C_\infty} \tag{12}$$

In the outlook of the above equations, the continuity (6) is satisfied whereas the (7) – (10) are transformed to second and third-order ordinary differential equations given below.

$$(1+\left((1-\Phi)+\Phi\Phi_1\right)(1-\Phi)^{2.5}\lambda_1 f'')f''' = \left((1-\Phi)+\Phi\Phi_1\right)(1-\Phi)^{2.5}(f'^2-(f+g)f'') + Mf'(1-\Phi)^{2.5}+Kf' \tag{13}$$

$$(1+\left((1-\Phi)+\Phi\Phi_1\right)(1-\Phi)^{2.5}\lambda_2 g'')g''' = \left((1-\Phi)+\Phi\Phi_1\right)(1-\Phi)^{2.5}(g'^2-(f+g)g'') + Mg'(1-\Phi)^{2.5}+Kg' \tag{14}$$

$$\left(\frac{k_{nf}}{k_f}+\frac{4}{3R}\right)\theta'' = -\Pr\left((f+g)\,\theta'((1-\Phi)+\Phi\Phi_2)\ +Q\theta\right) \tag{15}$$

$$\emptyset'' = -(Sc)\left(\sigma\,\emptyset\,(\theta\delta+1)^m \exp\left(\frac{-E}{1+\delta\theta}\right)-\emptyset'(f+g)\right) \tag{16}$$

Here $f, g, \emptyset, \theta$ *are the functions of* η and $\Phi_1 = \frac{\rho_s}{\rho_f}$, $\Phi_2 = \frac{(\rho C_p)_s}{(\rho C_p)_f}$

The corresponding boundary conditions are

$$at\ \ \eta = 0: \quad f'(\eta)=1,\ \ f(\eta)=0,\ \ g(\eta)=0,\ \ g'(\eta)=\propto,\ \ \theta'(\eta)=-Bi(1-\theta(\eta)),\ \ \emptyset(\eta)=1$$
$$at\ \ \eta\to\infty: \quad f'(\eta)\to 0,\ \ g'(\eta)\to 0 \qquad \theta(\eta)\to 0, \qquad \emptyset(\eta)\to 0 \tag{17}$$

where prime denotes the differentiation with respect to η. The associated non-dimensional parameters are $\lambda = \Gamma x\sqrt{a^3/2\nu}$, $\lambda_1 = \Gamma y\sqrt{a^3/2\nu}$, $M=\frac{\sigma B_0^2}{\rho_f a}$, $P_r = \frac{(\rho c_p)_f \nu_f}{K_f}$, $S_c = \frac{\nu_f}{D_B}$, $R = \frac{4\sigma^* T_\infty^3}{k^* K_f}$, $\alpha = \frac{b}{a}$, $\delta = \frac{T_w-T_\infty}{T_\infty}$, $\sigma = \frac{K_0^2}{a}$, $E = \frac{E_a}{kT_\infty}$, $Q = \frac{Q_o}{a(\rho c_p)_f}$ (18)

Interesting physical quantities in the present analysis are the heat transfer rates i.e., Nusselt numberNu, the Skin-friction coefficient C_f, and Sherwood number S_h (see for example [43], [59]) are defined as

$$C_{fx} = \frac{\tau_{xz}}{(\rho_f u_w^2)}, C_{fy} = \frac{\tau_{yz}}{(\rho_f v_w^2)}, \ Nu = \frac{-x\,q_w}{(T_w-T_\infty)}, \text{ and } S_h = \frac{-xJ_w}{(C_w-C_\infty)} \tag{19}$$

Here, $\tau_{xz} = \mu_{nf}\left[\frac{\partial u}{\partial z}+\frac{\Gamma}{\sqrt{2}}\left(\frac{\partial u}{\partial z}\right)^2\right]_{z=0}$, $\tau_{yz} = \mu_{nf}\left[\frac{\partial v}{\partial z}+\frac{\Gamma}{\sqrt{2}}\left(\frac{\partial v}{\partial z}\right)^2\right]_{z=0}$ represent shear stress at the surface, $q_w = -\left[k+\frac{16\,\sigma^* T_\infty^3}{3\,k^*}\right]\left(\frac{\partial T}{\partial z}\right)_{z=0}$ is the wall heat, and $J_w = -D\left(\frac{\partial C}{\partial z}\right)_{z=0}$ is the mass transfer. (20)

By using (19) and (20) the dimensionless "Skin-friction coefficient, Nusselt number, and Sherwood number" [65]-[68] are simplified as

$$\left.\begin{aligned} (Re_x)^{1/2}\,C_{fx} &= \frac{1}{(1-\Phi)^{2.5}}\left[f''(0)+\frac{\lambda}{2}\left(f''(0)\right)^2\right] \\ \propto^{3/2}(Re_x)^{1/2}\,C_{fy} &= \frac{1}{(1-\Phi)^{2.5}}\left[g''(0)+\frac{\lambda}{2}\left(g''(0)\right)^2\right] \\ (Re_x)^{-1/2}\,Nu_x &= -\left[\frac{k_{nf}}{k_f}+\frac{4}{3}R\right]\theta'(0) \\ (Re_x)^{-1/2}\,Sh &= -\emptyset'(0) \end{aligned}\right\} \tag{21}$$

$Re_x = \frac{u_w x}{\nu_f}$, $Re_y = \frac{v_w y}{\nu_f}$ are Reynold's numbers.

III. Numerical Method Validation

Using the shooting approach, numerical answers are derived for the given non-dimensional equations. The MATLAB built-in bvp5c function is then used to confirm the acquired results. The missing beginning

conditions are assumed in the firing technique and guided towards the boundary conditions using the RK-4 order method. The numerical bvp5c produced from the notion of a finite-difference scheme is used to compare the results.

$$f_1' = f_2, f_2' = f_3, and\ f_3' = \frac{((1-\Phi)+\Phi\Phi_1)(1-\Phi)^{2.5}(f_2{}^2-(f_1+f_4)f_3)+Mf_2(1-\Phi)^{2.5}+K f_2}{(1+((1-\Phi)+\Phi\Phi_1)(1-\Phi)^{2.5}\lambda f_3)} \quad (22)$$

$$f_4' = f_5, f_5' = f_6, and\ f_6' = \frac{((1-\Phi)+\Phi\Phi_1)(1-\Phi)^{2.5}(f_5{}^2-(f_1+f_4)f_6)+Mf_5(1-\Phi)^{2.5}+K f_5}{(1+((1-\Phi)+\Phi\Phi_1)(1-\Phi)^{2.5}\lambda f_6)} \quad (23)$$

$$f_7' = f_8, f_8' = -\frac{\Pr((f_1+f_4)f_8((1-\Phi)+\Phi\Phi_2)+Qf_7)}{\left(\frac{k_f}{k_{nf}}+\frac{4}{3R}\right)} \quad (24)$$

$$f_9' = f_{10}, f_{10}' = (Sc)\left(\sigma f_9 (f_7\delta+1)^m \exp\left(\frac{-E}{1+\delta f_7}\right) - (f_1+f_4)f_{10}\right) \quad (25)$$

The converted initial conditions are written as

$$f_2(0) = 1,\quad f_1(0) = 0,\quad f_4(0) = 0,\quad f_5 = \propto,\quad f_8 = -Bi(1-f_7),\quad f_9 = 1$$
$$f_2 \to 0,\qquad f_5 \to 0,\qquad f_7 \to 0,\qquad f_9 \to 0 \quad (26)$$

The governed (7) – (10) with boundary conditions (11) are tedious to solve analytically. Hence, solved them numerically in MATLAB using the bvp5c approach. The computations are initialized based on fixed values of physical parameters $\lambda_1=\lambda_2=0.2$, $\sigma=E=\delta=1.0$, Sc=0.6, Pr=6.2, R=K=M=Bi=α=0.5. The same base values may be assumed for the entire investigation as long as there is no particular indication. Finally, as a part of the validation of our computations, the cross-check of these results with the solutions of [28] and [69] (see Table II) is made and found that the results are in close agreement. Error tolerance of 10^{-5} is applied during the calculations, and all results are accurate within the set tolerance.

TABLE III: COMPARISON OF RESULTS OF SKIN FRICTION COEFFICIENTS ($C_f Re_x^{1/2}$) FOR DIFFERENT VALUES OF 'M' WHEN K = Λ1 = Λ2 = Φ = PR = R = Q = SC = E = σ = δ = A = M = 0

M	Present result	Reference [27]	Reference [70]
	$-C_f Re_x^{1/2}$	$-C_f Re_x^{1/2}$	$-C_f Re_x^{1/2}$
0	1.000008	1.00001	1.0000097
0.25	1.118022	1.11803	1.1180333
1	1.414213	1.41421	1.4142105
5	2.449490	2.44949	2.4494932
10	3.316625	3.31663	3.3166265
50	7.141428	7.14143	7.1414259
100	10.049875	10.0499	10.049894
500	22.383029	22.383	22.383134
1000	31.638584	31.6386	31.638602

IV. RESULTS AND DISCUSSION

Fig. 2-25 are graphical representations of several flow characteristics used to estimate momentum, energy, and mass species [27]. Tables IV and V also show the numerical values of skin friction coefficients, as well as the rate of heat and mass transfer coefficients [27].

TABLE IV: NUMERICAL DATA OF SKIN FRICTION COEFFICIENTS, NUSSELT NUMBER, AND SHERWOOD NUMBER [65]

M	K	λ_1	λ_2	α	Φ	$-C_f Re_x^{1/2}$	$-\propto^{3/2} C_f Re_y^{1/2}$	$Re_x^{-1/2} Nu$	$Re_x^{-1/2} Sh$
0.5	0.5	0.2	0.2	0.5	0.1	1.846368	0.861317	0.470978	0.918674
1						1.992866	0.945096	0.464355	0.913012
1.5						2.128336	1.021899	0.457615	0.908234
2						2.254757	1.093109	0.450747	0.904162
	1					2.034750	0.968902	0.462336	0.911488
	1.5					2.205507	1.065416	0.453492	0.905705
	2					2.362538	1.153508	0.444415	0.900980
		0.1				1.890029	0.863276	0.473018	0.920713
		0.3				1.803043	0.858680	0.468196	0.916022
		0.4				0.246337	0.861977	0.470557	0.918535
			0.1			1.846991	0.869563	0.471408	0.919088
			0.3			1.845681	0.852786	0.470506	0.918224
			0.4			1.844915	0.843984	0.469982	0.917728
				0.1		1.781614	0.151368	0.424338	0.886381
				0.3		1.814715	0.487421	0.452507	0.902335
				0.7		1.876576	1.266271	0.484185	0.934728
					0.2	2.400376	1.117445	0.603737	0.923067
					0.3	3.126542	1.467727	0.771618	0.930107
					0.4	4.181017	1.987184	0.990638	0.939203

TABLE V: NUMERICAL DATA OF NUSSELT NUMBER AND SHERWOOD NUMBER [65]

R	Pr	Bi	Q	Sc	E	δ	σ	m	$Re_x^{-1/2}Nu$	$Re_x^{-1/2}Sh$
1.2	6.2	0.3	0.2	0.6	0.1	1.0	1.0	0.3	0.470978	0.918674
0.3									0.128614	0.911789
2									0.733339	0.923792
3									1.027373	0.928631
	0.7								0.327614	0.942498
	4								0.426894	0.925975
	8								0.493723	0.915003
		1							0.972300	0.935643
		1.5							1.146659	0.941044
		2							1.259604	0.944425
			0.1						0.487614	0.916337
			0.3						0.446178	0.922151
			0.5						0.304095	0.941060
				0.2					0.470978	0.539057
				0.4					0.470978	0.744274
				0.8					0.470978	1.071834
					0.5				0.470978	0.817424
					1.5				0.470978	0.651366
					2				0.470978	0.603337
						0.5			0.470978	0.909806
						1.5			0.470978	0.926936
						2			0.470978	0.934679
							0.5		0.470978	0.738611
							1.5		0.470978	1.069858
							2		0.470978	1.202181
								0.5	0.470978	0.928535
								1.5	0.470978	0.982673
								2	0.470978	1.013051

Fig. 2-5 depict the impact of local Williamson parameters λ_1 and λ_2 on velocity, temperature, and concentration profiles. It is noticed that, as the parameter λ_1 rises, the axial velocity falls while the transverse velocity increases (see Fig. 2). In practice, the Williamson parameter is directly proportional to the relaxation time [28]; hence, the rise in the Williamson parameter corresponds to a rise in the ion relaxation time intern it generates an increase in fluid viscosity, which causes a decrease in velocity. With the impact of λ_2, a completely different trend is observed (see Fig. 3). The decrease in fluid velocity results in the reduction in heat transfer from the fluid. As a result, the fluid temperature rises and the same can be seen in Fig. 4. Williamson parameter causes the growth of viscosity of the nanofluid, thereby the concentration flow of GaN nanoparticles increases (Fig. 5).

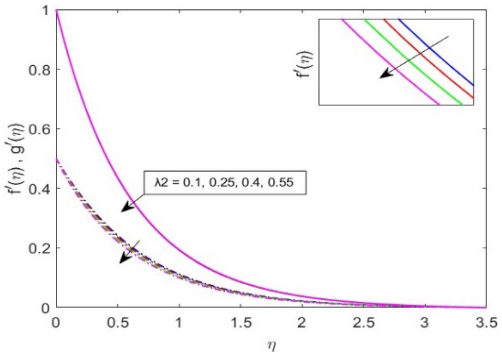

Fig. 2. Role of λ_1 on the velocity profiles.

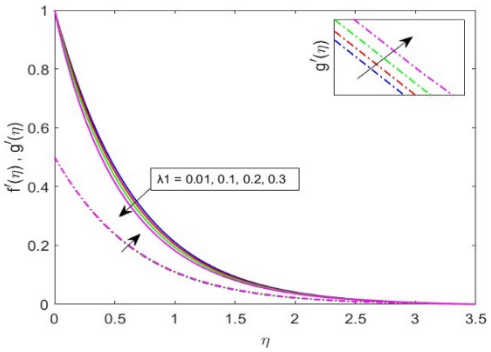

Fig. 3. Role of $\lambda 2$ on the velocity profiles.

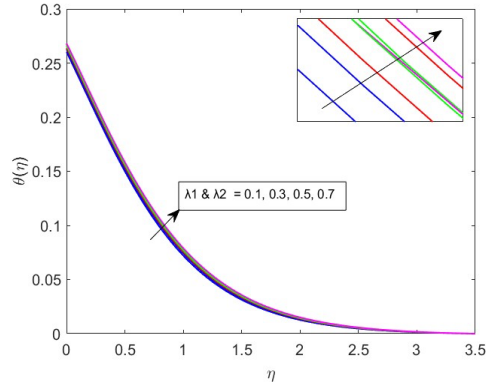

Fig. 4. Role of λ_1 & λ_2 on temperature profiles.

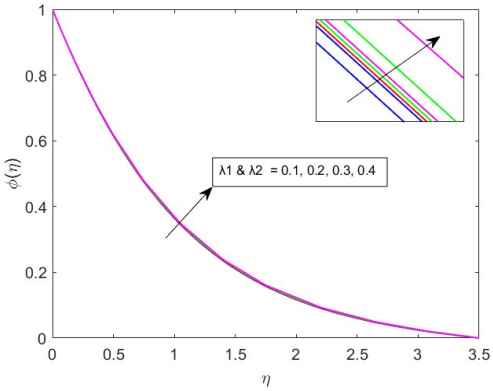

Fig. 5. Role of λ_1 & λ_2 on concentration profiles.

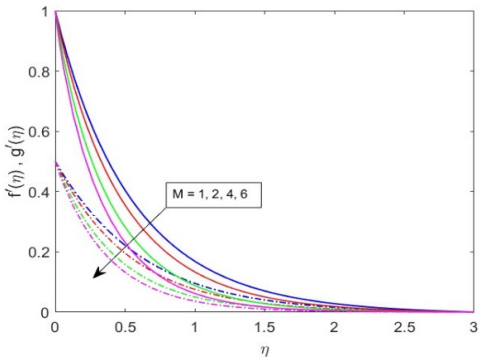

Fig. 6. Role of *M* on velocity profiles.

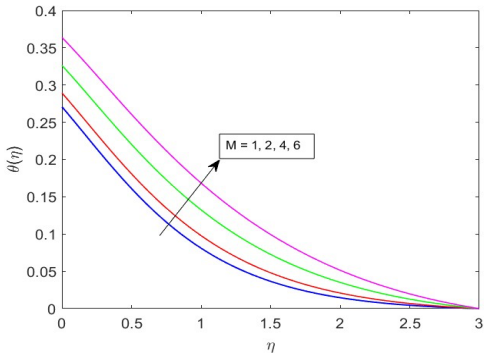

Fig. 7: Role of *M* on temperature profiles.

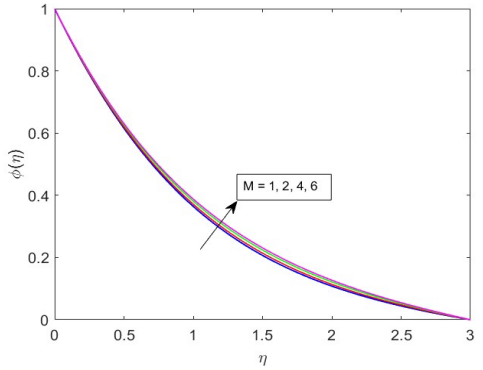

Fig. 8. Role of *M* on concentration profiles.

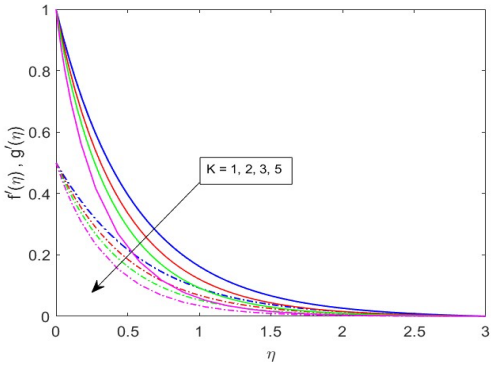

Fig. 9. Role of *K* on velocity profiles.

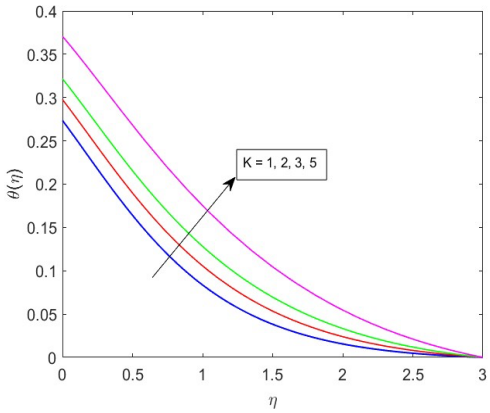

Fig. 10. Role of *K* on temperature profiles.

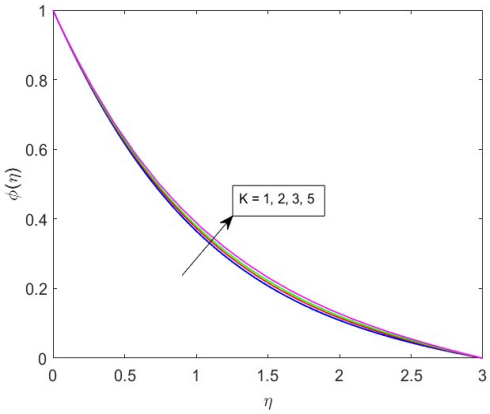

Fig. 11. Role of *K* on concentration profiles.

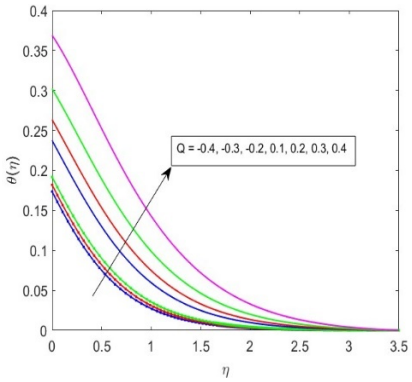

Fig. 12. Role of *Q* on the temperature profile.

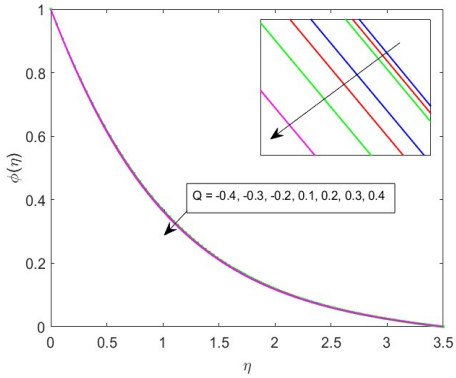

Fig. 13. Role of *Q* on concentration profile.

Fig. 6 shows the reduced velocities of both axial and transverse with the increase in the magnetic field. This is because of the Lorentz force that arises with the increase in the applied magnetic field and this force resists the fluid flow and causes a reduction in both the velocities. Also, the Lorentz force causes internal friction among the particles in the fluid hence fluid temperature increases with the applied magnetic field [28]. The temperature and concentration profiles of GaN + Ethylene glycol nanofluid are shown in Fig. 7 and 8. The graphs indicate the rise in temperature also the rise in concentration. It can be seen from Fig. 9

that as the porosity parameter increases, the axial and transverse velocities as well as the related momentum boundary layer thickness decrease. This is because the increasing porosity generates higher fluid permeability along Z-direction, which increases fluid velocity in this direction i.e. –ve Z-direction in particular. As a result, both the velocities of the fluid flow are reduced. The porosity parameter, on the other hand, produces a rise in temperature and concentration. Fig. 10 and 11 show this clearly in the case of fluid containing GaN nanoparticles.

The influence of heat source/sink is represented by a non-dimensional parameter Q *($Q>0$ for source, $Q<0$ for sink)*, on the variation of temperature profile (drawn between $\theta(\eta)$ and η) and on concentration profile (drawn between $\emptyset(\eta)$ and η) for different values of Q keeping other dimensionless parameters as constant are shown in Fig. 12 and 13. As the value of Q increases from -Q *(sink) to* +Q*(source),* the temperature profile is enhanced and the concentration profile is diminished in the case of source/sink, as a result, the thermal boundary layer thickness increases. Physically, a heat source can add more heat to the boundary layer region, increasing the thickness of the thermal bound layer and decreasing the heat transfer rate from the surface to the fluid. Reference [61] observed similar results while numerically simulating the constant laminar MHD hybrid nanofluid flow and heat transfer via an exponentially expanding or decreasing sheet in a porous medium and [17] while studying the three-dimensional hydromagnetic convective flow of chemically reactive Williamson fluid with non-uniform heat absorption and generation.

"The stretching rate parameter α is the ratio of the transverse velocity to the axial velocity". In general, the porosity parameter reduces fluid velocity, resulting in high concentration. It signifies that the increase in a porous sheet's stretching parameter that the transverse velocity outnumbers the axial velocity [28]. Henceforth, the rise in the value of α causes a rise in the transverse velocity and simultaneously, a decrease in the axial velocity. This trend is clearly shown in Fig. 14. The stretching rate parameter α, also causes a decrease in the temperature and concentration profiles (Fig 15 and 16).

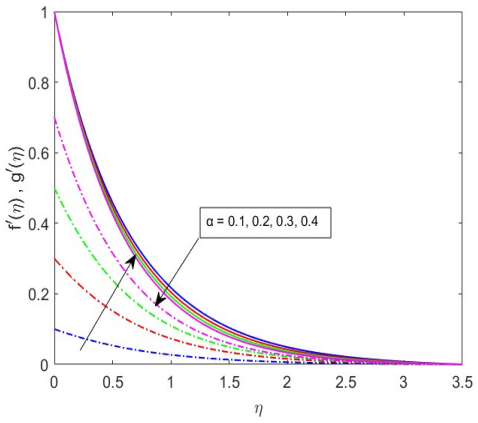

Fig.14: Role of α on velocity profiles.

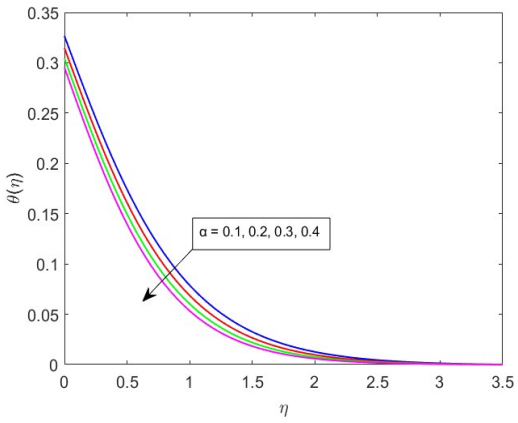

Fig. 15. Role of α on temperature profiles.

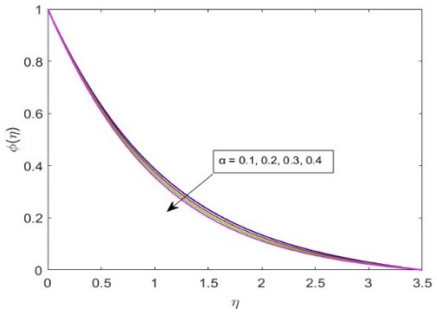

Fig. 16. Role of α on concentration fields.

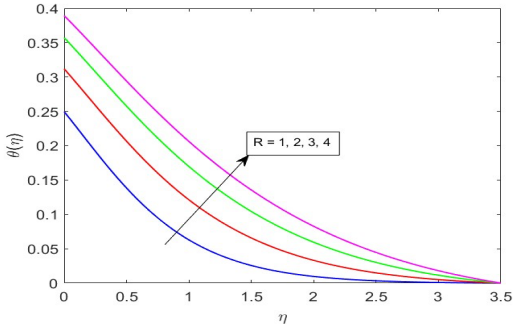

Fig. 17. Role of R on temperature profiles.

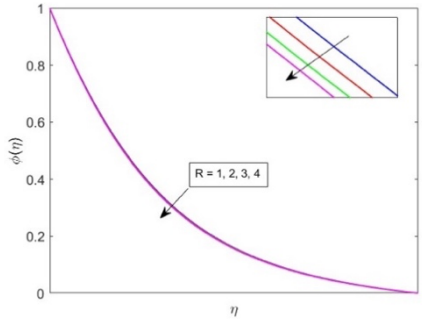

Fig. 18. Role of R on concentration profile.

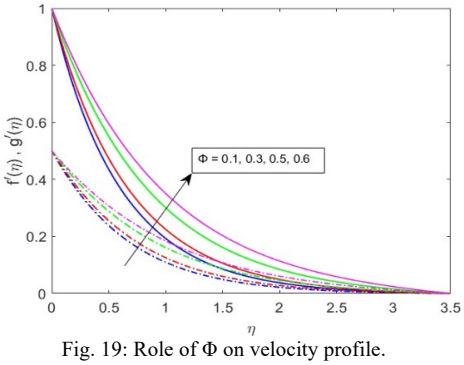

Fig. 19: Role of Φ on velocity profile.

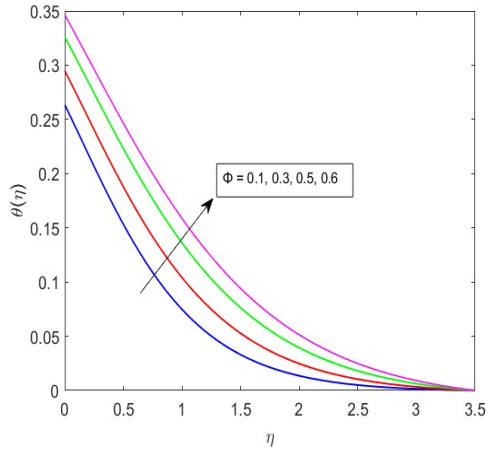

Fig. 20. Role of Φ on the temperature profile.

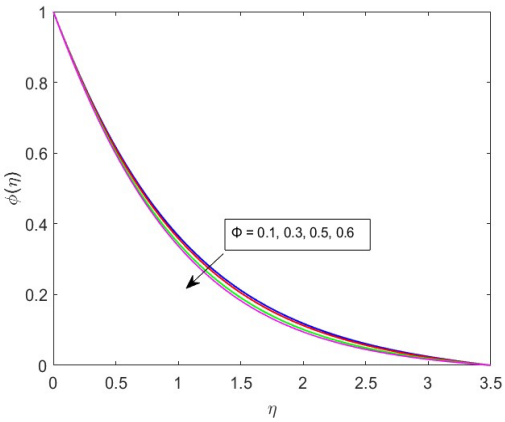

Fig. 21. Role of Φ on concentration profile.

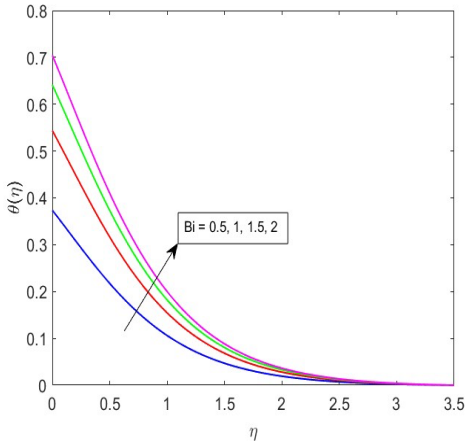

Fig. 22. Role of *Bi* on temperature profile.

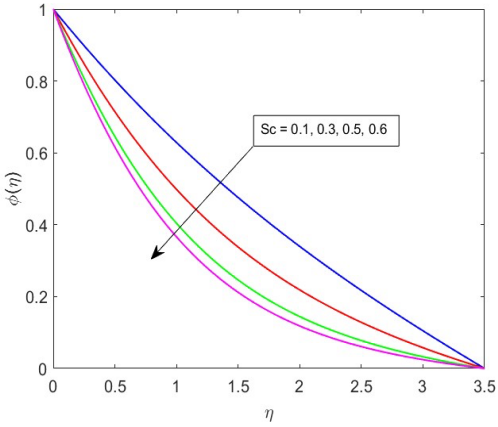

Fig. 23: Role of *Sc* on concentration profile.

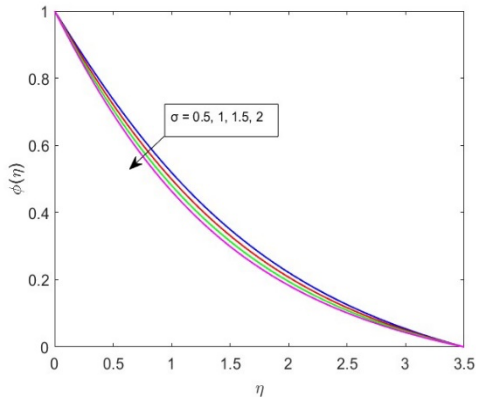

Fig. 24. Role of σ on concentration profile.

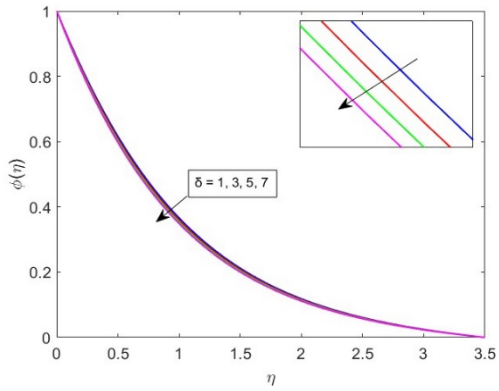

Fig. 25: Role of δ on concentration profile.

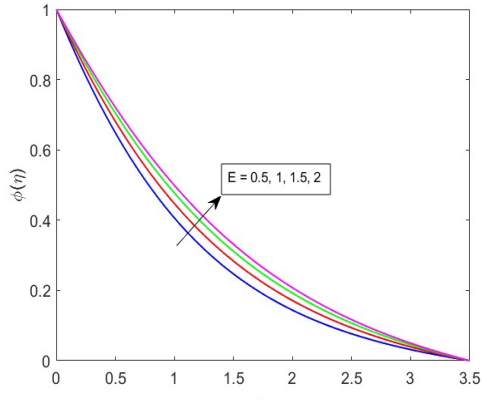

Fig. 26. Role of *E* on concentration profile.

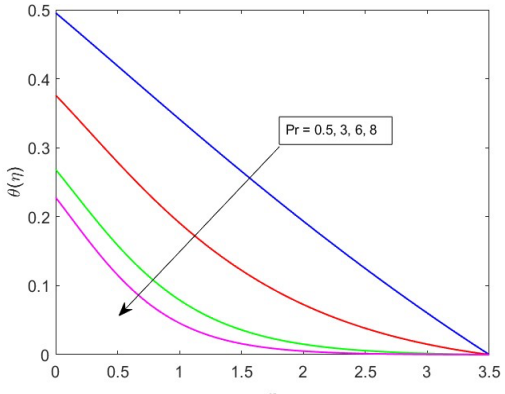

Fig. 27. Role of *Pr* on the temperature profile.

Thermal radiation, the strength of which is represented in terms of radiation parameter *R*, applied to a nanofluid, enhances the fluid temperature and boundary layer thickness with the increase in parameter R. This result, observed in the nanofluid consisting of GaN nanoparticles mixed with Ethylene glycol is shown clearly in Fig. 17. Thermal radiation adds heat to the working fluid, causing the fluid temperature to rise. It is worth mentioning that the concentration field decreases with the increase in thermal radiation (Fig. 18) as a result of the random movement of fluid molecules.

Fig. 19, 20 and 21 show the characterization of the nanofluid volume fraction Φ on different velocities, temperature, and concentration profiles. It is observed that when Φ increases, so does the velocity profile along the axial and transverse axes (Fig. 19). With the same order of Φ, the resistance force within the fluid increases, while the temperature profiles exhibit opposite behavior (Fig. 20). This is because the thermal conductivity and thickness of the thermal boundary layer decrease as Φ increases. A similar result was also observed in Al_2O_3-water nanofluids by [71]. It is obvious from Fig. 21 that the concentration profile of GaN-Ethylene glycol nanofluid decreases. A similar observation was also made by [72] in SWCNT-water nanofluids. According to them the observed decrease in concentration profile is due to the stronger diffusion boundary layer thickness that the SWCNT-water nanofluids have when compared to Cu-water fluids since the carbon nanotubes have extraordinary mechanical, electrical, thermal, optical, and chemical properties[72]. Nanofluid, under the present study, has GaN nanoparticles of very good optical, electrical and chemical properties, due to the nitride present in the compound, the fluid may also be assigned with a strong diffusion boundary layer thickness responsible for the decrease in concentration profile.

The temperature profile of GaN-Ethylene glycol nanofluid accelerates with the increasing of thermal Biot number *Bi* and the same is noted in Fig. 22. In general, the thermal Biot number describes convection. As the Biot number grows convection improves. As a result of the increasing thermal Biot number, the fluid temperature increases. Fig. 23 depicts the graphical variation between species concentration and Schmidt number Sc. It is obvious from the figure that the nanoparticle concentration decreases with the increase in Sc. This is because the Schmidt number varies inverse proportion to the rate of diffusion of mass [28]. Therefore, diffusion of mass decreases as the Schmidt number increases.

According to Fig. 24, the species (GaN nanoparticles) concentration falls as the boundary layer thickness of the solute (Ethylene glycol) decreases as a result of the increase in chemical reaction parameter σ. Practically, the diffusivity of the fluid varies due to the change in intensity of the chemical reaction, and thus the concentration declines. Reference [72] discovered that when the chemical reaction and buoyancy ratio increased, the concentration of water-based SWCNTs, Cu, and Al_2O_3 decreased, but the rate of mass transfer increased due to the combined impact of diffusion conductivity and kinematic viscosity of the nanoparticles. They also discovered that the diffusion boundary layer thickness of water-base Cu and SWCNTs increases faster than that of Al_2O_3-water as the chemical reaction progresses [72].

Fig. 25 explores the effect of temperature difference parameter δ on the concentration field of GaN-Ethylene glycol nanofluid. The temperature difference parameter δ is defined as the difference between surface and ambient temperatures. When δ grows, the concentration boundary layer thickness increases, resulting in a decrease in the concentration field. A similar observation i.e. decrease of concentration field as a result of the increase in δ was also made on Maxwell-Sutterby fluid by [73].

The impact of Arrhenius activation parameter *E* on the concentration profiles of GaN-Ethylene glycol nanofluid is illustrated in Fig. 26. Truly, *E* is the energy that must be used to proceed with the chemical reaction. It is also defined as the least amount of energy necessary to initiate and sustain a chemical reaction. It is a general observation that the increase in the activation energy causes an increase in the nanoparticle concentration. Reference [74] have studied the "Impacts of chemical reaction with activation energy on the unsteady flow of magneto-Williamson nanofluids and concluded that an increase in the destructive chemical reaction parameter $\boldsymbol{\sigma} > 0$ tends to reduce the nanoparticle concentration profile" [74]. The simulated concentration profiles for various temperature difference parameter δ were also studied in the presence and absence of a magnetic field and it has been concluded that the concentration profile curves exhibited a decreasing trend with higher values of the temperature difference parameter, as well as a general trend of increase in the nanoparticle concentration profile with the rise in activation energy *E* [74].

Fig. 27 is drawn to understand the influence of Prandtl number *Pr* on the temperature profiles of GaN-Ethylene glycol nanofluid. "Prandtl number *Pr* is defined as the ratio of momentum diffusivity to the thermal diffusivity". According to the fundamental definition of Pr, increasing thermal diffusivity results in a decrease in the Prandtl number, which depreciates the temperature field [73]. This type of behavior appears to be common in most nanofluids because several research articles on nanofluids with different nanoparticles in different base fluids appear in the literature [52], [75], [76].

V. Conclusion

In this paper, a numerical analysis of a 3-D Williamson MHD fluid of Ethylene glycol added with Gallium Nitride semiconductor nanoparticles over a linearly stretching porous sheet with heat source/sink, radiation, and Arrhenius activation energy was presented. MATLAB built-in bvp5c function was used for the computational analysis. Numerical data of Skin friction coefficient, Nusselt number, and Sherwood numbers were used for the confirmation of obtained results.

- A rise in the axial velocities and decrease in the transverse velocities with Williamson constants λ_1 and exactly a reverse effect with Williamson constants λ_2 is observed. The temperature and concentration profiles increase with the increase in Williamson fluid parameters.
- Both axial and transverse velocities decrease whereas the temperature and concentration profiles increase with the increase in the magnetic field and porosity parameters.
- Axial/transverse velocities decrease/increase and temperature & concentration profiles decrease with the increase in stretching ratio parameter.
- The influence of heat source and sink is such that the temperature of the nanofluid increases
- The temperature profile shows enhancing behavior with an increase in radiation parameters.
- Velocity and temperature profiles show an increasing and the concentration profile decreasing trends with the increase in volume fraction.
- The temperature profile grows with an increase in Biot number and reduces with an increase in Prandtl number.
- The concentration profile decreases with an increase in Schmidt number, fitted rate constant, chemical reaction, and temperature difference parameters.
- The concentration profile increases with an increase in the activation energy parameter.

Nomenclature

τ: extra stress tensor, S: Cauchy stress tensor, I: identity vector, P: pressure, μ_0: limiting viscosity at zero shear rate, A_1: first Rivlin- Erickson tensor, μ_∞: Limiting viscosity at infinity shear rate, Γ: Time constant, ρ_{nf}: Nanofluid density, σ: Electric conductivity, B_o: Magnetic field strength, μ_{nf}: Dynamic viscosity of the nanofluid, T: Temperature of the fluid, C: Concentration of the fluid, Q_o: Heat source/sink, α_{nf}: Thermal diffusivity, D_B: Diffusion coefficient, K_p: Permeability of the porous medium, c_p: Specific heat at constant pressure, σ^*: Stefan Boltzmann constant, k^*: Mean absorption coefficient, α_{nf}: Thermal diffusivity, K_o : Chemical reaction constant, E_a: Activation energy parameter, k: Boltzmann constant, m: Fitted rate constant, Γ: Williamson fluid parameter, ρ: Density, λ_1 & λ_2: Williamson parameters, M: Magnetic parameter, P_r: Prandtl number, Q: Heat source/sink parameter, S_c Schmidt number, R: Radiation parameter, ∝: Stretching ratio parameter, δ: Temperature difference parameter, σ: Chemical reaction parameter, E: Activation energy parameter.

Acknowledgment

The authors would like to thank the Head, Department of Mathematics, University College of Science, Osmania University, Hyderabad, India for his participation in the discussions and help. One of the authors M. Jyotshna thanks the Principal and Head, Department of Applied Sciences and Humanities, Maturi Venkata Subba Rao Engineering College, Nadergul, Hyderabad for their constant encouragement and support in conducting the research work.

Conflict of Interest

Authors declare that they do not have any conflict of interest.

References

[1] Bilal S, Khalil-ur-R, Malik MY, Hussain A, Khan M. Effects of temperature dependent conductivity and absorptive/generative heat transfer on MHD three dimensional flow of Williamson fluid due to bidirectional non-linear stretching surface. *Results Phys.* 2017; 7: 204–212.
[2] Nandeppanavar MM, Vaishali S, Kemparaju MC, Raveendra N. Theoretical analysis of thermal characteristics of casson nano fluid flow past an exponential stretching sheet in Darcy porous media. *Case Stud. Therm. Eng.* 2020; 21: 100717.
[3] Nandeppanavar MM, Vajravelu K, Subhas Abel M. Heat transfer in MHD viscoelastic boundary layer flow over a stretching sheet with thermal radiation and non-uniform heat source/sink. *Commun. Nonlinear Sci. Numer. Simul.* 2011; 16(9): 3578–3590.
[4] Das SK, Choi SUS Patel HE. Heat transfer in nanofluids - A review. *Heat Transf. Eng.* 2006; 27(10): 3–19.
[5] Xuan Y, Li Q. Heat transfer enhancement of nanofluids. *Int. J. Heat Fluid Flow*. 2000; 21(1): 58–64.

[6] Wong KV, De Leon O. Applications of nanofluids: Current and future. *Adv. Mech. Eng.* 2010; 2010.
[7] Choi S. Nanofluid technology: current status and future research. *Energy*. 1998: 26.
[8] Khan NA, Khan H. A Boundary layer flows of non-Newtonian Williamson fluid. *Nonlinear Eng.* 2014; 3(2): 107–115.
[9] Nadeem S, Hussain ST. Analysis of MHD Williamson nano fluid flow over a heated surface. *J. Appl. Fluid Mech.* 2016; 9(2): 729–739.
[10] Kurtcebe C, Erim MZ. Heat transfer of a non-newtonian viscoinelastic fluid in an axisymmetric channel with a porous wall for turbine cooling application. *Int. Commun. Heat Mass Transf.* 2002; 29(7): 971-982.
[11] Ibrahim W, Shankar B. MHD boundary layer flow and heat transfer of a nanofluid past a permeable stretching sheet with velocity, thermal and solutal slip boundary conditions. *Comput. Fluids*. 2013; 75: 1-10.
[12] Sheikholeslami M, Shehzad SA, Li Z, Shafee A. Numerical modeling for alumina nanofluid magnetohydrodynamic convective heat transfer in a permeable medium using Darcy law. *Int. J. Heat Mass Transf.* 2018; 127: 614–622.
[13] Eid MR, Al-Hossainy AF. Synthesis, DFT calculations, and heat transfer performance large-surface TiO2: ethylene glycol nanofluid and coolant applications. *Eur. Phys. J. Plus*. 2020; 135(7).
[14] Eid MR. Effects of NP Shapes on Non-Newtonian Bio-Nanofluid Flow in Suction/Blowing Process with Convective Condition: Sisko Model. *J. Non-Equilibrium Thermodyn.* 2020; 45(2): 97–108.
[15] Kotresh MJ, Ramesh GK, Shashikala VKR, Prasannakumara BC. Assessment of Arrhenius activation energy in stretched flow of nanofluid over a rotating disc. *Heat Transf.* 2021; 50(3): 2807–2828.
[16] Mallikarjuna HB, Nirmala T, Punith Gowda RJ, Manghat R, Varun KumarTw RS. Two-dimensional Darcy–Forchheimer flow of a dusty hybrid nanofluid over a stretching sheet with viscous dissipation. *Heat Transf.* 2021; 50(4): 3934–3947.
[17] Jayadevamurthy PGR, Kumar Rangaswamy N, Prasannakumara BC, Nisar KC. Emphasis on unsteady dynamics of bioconvective hybrid nanofluid flow over an upward–downward moving rotating disk. *Numer. Methods Partial Differ. Equ.*. 2020: 1–22.
[18] Al-Hossainy AF, Eid MR. Structure, DFT calculations and heat transfer enhancement in [ZnO/PG + H2O]C hybrid nanofluid flow as a potential solar cell coolant application in a double-tube. *J. Mater. Sci. Mater. Electron.* 2020; 31(18): 15243–15257.
[19] Prasannakumara BC, Gireesha BJ, Krishnamurthy MR, Ganesh Kumar K. MHD flow and nonlinear radiative heat transfer of Sisko nanofluid over a nonlinear stretching sheet. *Informatics Med. Unlocked*. 2917; 9(August): 123–132.
[20] Qayyum S, Khan MI, Chammam W, Khan WA, Ali Z, Ul-Haq W. Modeling and theoretical investigation of curved parabolized surface of second-order velocity slip flow: Combined analysis of entropy generation and activation energy. *Mod. Phys. Lett. B*. 2020; 34(33): 1–15.
[21] Qayyum S, Hayat T, Alsaedi A. Thermal radiation and heat generation/absorption aspects in third grade magneto-nanofluid over a slendering stretching sheet with Newtonian conditions. *Phys. B Condens. Matter*. 2018; 537: 139–149.
[22] Hayat T, Kiyani MZ, Alsaedi A, Ijaz Khan M, Ahmad I. Mixed convective three-dimensional flow of Williamson nanofluid subject to chemical reaction. *Int. J. Heat Mass Transf.* 2018; 127: 422–429.
[23] Malik S, Bilal MY, Khalil-ur-R, Hussain A, Khan M. Effects of temperature dependent conductivity and absorptive/generative heat transfer on MHD three dimensional flow of Williamson fluid due to bidirectional non-linear stretching surface. *Results Phys.* 2017; 7: 204–212.
[24] Malik MY, Bilal S, Salahuddin T, Rehman KU. Three-Dimensional Williamson Fluid Flow over a Linear Stretching Surface. *Math. Sci. Lett.* 2017; 6(1): 53–61.
[25] Wang CY. The three-dimensional flow due to a stretching flat surface. *Phys. Fluids*. 1984; 27(8): 1915–1917.
[26] Mahanthesh B, Gireesha BJ, Gorla RSR, Makinde OD. Magnetohydrodynamic three-dimensional flow of nanofluids with slip and thermal radiation over a nonlinear stretching sheet: a numerical study. *Neural Comput. Appl*. 2018; 30(5): 1557–1567.
[27] Alaidrous AA, Eid MR. 3-D electromagnetic radiative non-Newtonian nanofluid flow with Joule heating and higher-order reactions in porous materials. *Sci. Rep.* 2020; 10(1): 1–19.
[28] Geethan KS, Varma SVK, Kiran Kumar RVMSS, Raju CSK, Shehzad SA, Bashir MN. Three-dimensional hydromagnetic convective flow of chemically reactive williamson fluid with non-uniform heat absorption and generation. *Int. J. Chem. React. Eng.* 2019; 17(2): 1–17.
[29] Nainaru T, Narayana PVS, Venkateswarlu B. Numerical simulation of variable thermal conductivity on 3D flow of nanofluid over a stretching sheet. *Nonlinear Eng.* 2020; 9(1): 233–243.
[30] Thumma T, Mishra SR, Abbas MA, Bhatti MM, Abdelsalam SI. Three-dimensional nanofluid stirring with non-uniform heat source/sink through an elongated sheet. *Appl. Math. Comput.* 2022; 421: 126927.
[31] Hemmat Esfe M, Motallebi SM, Bahiraei M. Employing response surface methodology and neural network to accurately model thermal conductivity of TiO2–water nanofluid using experimental data. *Chinese J. Phys.* 2021; 70(December): 14–25.
[32] Hayat T, Waqas M, Khan MI, Alsaedi A. Analysis of thixotropic nanomaterial in a doubly stratified medium considering magnetic field effects. *Int. J. Heat Mass Transf.* 2016; 102: 1123–1129.
[33] Farooq M, Khan MI, Waqas M, Hayat T, Alsaedi A, Khan MI. MHD stagnation point flow of viscoelastic nanofluid with non-linear radiation effects. *J. Mol. Liq.* 2016; 221: 1097–1103.
[34] Hayat T, Khan MWA, Khan MI, Waqas M, Alsaedi A. Impact of chemical reaction in fully developed radiated mixed convective flow between two rotating disk. *Phys. B Condens. Matter*. 2018; 538(February): 138–149.
[35] Hayat T, Khan MI, Waqas M, Alsaedi A, Yasmeen T. Diffusion of chemically reactive species in third grade fluid flow over an exponentially stretching sheet considering magnetic field effects. *Chinese J. Chem. Eng.* 2017; 25(3): 257–263.
[36] Waqas M, Farooq M, Khan MI, Alsaedi A, Hayat T, Yasmeen T. Magnetohydrodynamic (MHD) mixed convection flow of micropolar liquid due to nonlinear stretched sheet with convective condition. *Int. J. Heat Mass Transf.* 2016; 102: 766–772.
[37] Hayat T, Muhammad T, Alsaedi A, Alhuthali MS. Magnetohydrodynamic three-dimensional flow of viscoelastic nanofluid in the presence of nonlinear thermal radiation. *J. Magn. Magn. Mater.* 2015; 385: 222–229.
[38] Gireesha BJ, Gorla RSR, Mahanthesh B. Effect of Suspended Nanoparticles on Three-Dimensional MHD Flow, Heat and Mass Transfer of Radiating Eyring-Powell Fluid Over a Stretching Sheet. *J. Nanofluids*. 2015; 4(4): 474–484.
[39] Bachok N, Ishak A, Nazar R, Pop I. Flow and heat transfer at a general three-dimensional stagnation point in a nanofluid. *Phys. B Condens. Matter*. 2010; 405(24): 4914–4918.
[40] Khan JA, Mustafa M, Hayat T, Alsaedi A. Three-dimensional flow of nanofluid over a non-linearly stretching sheet: An application to solar energy. *Int. J. Heat Mass Transf.* 2015; 86: 158–164.
[41] Wang W, Zhang B, Cui L, Zheng H, Klemeš JJ, Wang J. Numerical study on heat transfer and flow characteristics of nanofluids in a circular tube with trapezoid ribs. *Open Phys.* 2021; 19(1): 224–233.
[42] Muhammad N, Nadeem S. Ferrite nanoparticles Ni- ZnFe2O4 , Mn- ZnFe2O4 and Fe2O4 in the flow of ferromagnetic nanofluid. *Eur. Phys. J. Plus*. 2017; 132(9).
[43] Ramzan M, Gul H, Zahri M. Darcy-Forchheimer 3D Williamson nanofluid flow with generalized Fourier and Fick's laws in a stratified medium. *Bull. Polish Acad. Sci. Tech. Sci.* 2020; 68(2): 327–335.
[44] Omiddezyani S, Gharehkhani S, Yousef-Asli V, Khazaee I, Ashjaee M, Nayebi R, et al. Experimental investigation on thermo-physical properties and heat transfer characteristics of green synthesized highly stable CoFe2O4/rGO nanofluid. *Colloids Surfaces A Physicochem. Eng. Asp.* 2021; 610(November): 125923.

[45] Sheikh NA, Ching DL, Khan I, Sakidin HB, Jamil M, Khalid HU, Ahmed N. Fractional model for MHD flow of Casson fluid with cadmium telluride nanoparticles using the generalized Fourier's law. *Sci. Rep.* 2021; 11(1): 1–21.
[46] Kameswaran PK, Sibanda P, Murti ASN. Nanofluid flow over a permeable surface with convective boundary conditions and radiative heat transfer. *Math. Probl. Eng.* 2013; 2013.
[47] Bachok N, Ishak A, Pop I. Boundary layer stagnation-point flow and heat transfer over an exponentially stretching/shrinking sheet in a nanofluid. *Int. J. Heat Mass Transf.* 2012; 55(25-26): 8122–8128.
[48] Mandal G. Convective-Radiative Heat Transfer of Micropolar Nanofluid Over a Vertical Non-Linear Stretching Sheet. *J. Nanofluids*. 2016; 5(6): 852–860.
[49] Mandal S, Shit GC. Entropy analysis of unsteady MHD three-dimensional flow of Williamson nanofluid over a convectively heated stretching sheet. *Heat Transf.* 2022; 51(2): 2034–2062.
[50] Swain K, Mahanthesh B. Thermal Enhancement of Radiating Magneto-Nanoliquid with Nanoparticles Aggregation and Joule Heating: A Three-Dimensional Flow. *Arab. J. Sci. Eng.* 2021; 46(6): 5865–5873.
[51] Siddiqui AA, Sheikholeslami M. TiO2-water nanofluid in a porous channel under the effects of an inclined magnetic field and variable thermal conductivity. *Appl. Math. Mech.* 2018; 39(8): 1201–1216.
[52] Nayak MK, Prakash J, Tripathi D, Pandey VS. 3D radiative convective flow of ZnO-SAE50nano-lubricant in presence of varying magnetic field and heterogeneous reactions. *Propuls. Power Res.* 2019; 8(4): 339–350.
[53] Yacob NA, Dasman A, Ahmad S. Regional Conference on Science, Technology and Social Sciences (RCSTSS 2016). *Reg. Conf. Sci. Technol. Soc. Sci. (RCSTSS 2016)*. 2018.
[54] Zhao Z, Buscaglia V, Vivani M, Buscaglia MT, Mitoseriu L, Testion A, et al. Grain-size effects on the ferroelectric behavior of dense nanocrystalline BaTiO3 ceramics. *Phys. Rev. B.* 2004; 70(2).
[55] Hreniak D, Strek W, Amami J, Guyot Y, Boulon G, Goutaudier C, et al. The size-effect on luminescence properties of BaTiO3:Eu 3+ nanocrystallites prepared by the sol-gel method. *J. Alloys Compd.* 2004; 380(1-2): 348–351.
[56] Hreniak D, Stręk W. Synthesis and optical properties of Nd3+-doped Y 3Al5O12 nanoceramics. *J. Alloys Compd.* 2002; 341(1-2): 183–186.
[57] Nadeem S, Hussain ST, Lee C. Flow of a williamson fluid over a stretching sheet. *Brazilian J. Chem. Eng.* 2013; 30(3): 619–625.
[58] Shawky HM, Eldabe NTM, Kamel KA, Abd-Aziz EA. MHD flow with heat and mass transfer of Williamson nanofluid over stretching sheet through porous medium. *Microsyst. Technol.* 2019; 25(4): 1155–1169.
[59] Sultan F, Khan WA, Ali M, Shahzad M, Irfan M, Khan M. Theoretical aspects of thermophoresis and Brownian motion for three-dimensional flow of the cross fluid with activation energy. *Pramana - J. Phys.* 2019; 92(2): 1–10.
[60] Khashi'ie NS, Arifin NM, Pop I, Nazar R, Hafidzuddin EH, Wahi N. Three-Dimensional Hybrid Nanofluid Flow and Heat Transfer past a Permeable Stretching/Shrinking Sheet with Velocity Slip and Convective Condition. *Chinese J. Phys.* 2020; 66: 157–171.
[61] Eid MR, Nafe MA. Thermal conductivity variation and heat generation effects on magneto-hybrid nanofluid flow in a porous medium with slip condition. *Waves in Random and Complex Media*. 2022; 32(3): 1103–1127.
[62] Mion C, Muth JF, Preble EA, Hanser D. Thermal conductivity, dislocation density and GaN device design. *Superlattices and Microstructures*. 2006; 40(4-6): 338-342.
[63] Krukowski S, Witek A, Adamczyk J, Jun J, Bockowski M, Grzegory I, Lucznik B, Nowak G, Wróblewski M, Presz A, Gierlotka S. Thermal properties of indium nitride. *Journal of Physics and Chemistry of Solids.* 1998; 59(3): 289-95.
[64] Sreedevi P, Sudarsana Reddy P. Effect of magnetic field and thermal radiation on natural convection in a square cavity filled with TiO2 nanoparticles using Tiwari-Das nanofluid model. *Alexandria Eng. J.* 2022; 61(2): 1529–1541.
[65] Nandi S, Kumbhakar B. Viscous Dissipation and Chemical Reaction Effects on Tangent Hyperbolic Nanofluid Flow Past a Stretching Wedge with Convective Heating and Navier's Slip Conditions. *Iran. J. Sci. Technol. - Trans. Mech. Eng.* 2021; 46(2): 379–397.
[66] Laxmi TV, Shankar B. Effect of Nonlinear Thermal Radiation on Boundary Layer Flow of Viscous Fluid over Nonlinear Stretching Sheet with Injection/Suction. *J. Appl. Math. Phys.* 2016; 4(2): 307–319.
[67] Srinivasulu T, Goud BS. Effect of inclined magnetic field on flow, heat and mass transfer of Williamson nanofluid over a stretching sheet. *Case Stud. Therm. Eng.* 2021; 23(October): 100819.
[68] Rushi B, Sivaraj KR, Prakash J. Editors. *Lecture Notes in Mechanical Engineering Advances in Fluid Dynamics*. [Internet]. 2018. Available: http://www.springer.com/series/11693
[69] Ariel PD. Generalized three-dimensional flow due to a stretching sheet. *ZAMM Zeitschrift fur Angew. Math. und Mech.* 2003; 83(12): 844–852.
[70] Oyelakin IS, Lalramneihmawii P, Mondal S, Nandy SK, Sibanda P. Thermophysical analysis of three-dimensional magnetohydrodynamic flow of a tangent hyperbolic nanofluid. *Eng. Reports*. 2020; 2(4): 1–13.
[71] Ogunseye HA, Mondal H, Sibanda P, Mambili-Mamboundou H. Lie group analysis of a Powell–Eyring nanofluid flow over a stretching surface with variable properties. *SN Appl. Sci.* 2020; 2(1): 1–12.
[72] Kandasamy R, Mohamad R, Ismoen M. Impact of chemical reaction on Cu, Al2O3 and SWCNTs–nanofluid flow under slip conditions. *Eng. Sci. Technol. an Int. J.* 2016; 19(2): 700–709.
[73] Sajid T, Tanveer S, Sabir Z, Guirao JLG. Impact of Activation Energy and Temperature-Dependent Heat Source/Sink on Maxwell-Sutterby Fluid. *Math. Probl. Eng.* 2020; 2020.
[74] Hamid A, Khan M. Impacts of binary chemical reaction with activation energy on unsteady flow of magneto-Williamson nanofluid. *J. Mol. Liq.* 2018; 262: 435–442.
[75] Hayat T, Shah F, Khan MI, Khan MI, Alsaedi A. Entropy analysis for comparative study of effective Prandtl number and without effective Prandtl number via γAl2O3-H2O and γAl2O3-C2H6O2 nanoparticles. *J. Mol. Liq.* 2018; 266: 814–823.
[76] Hussain ST, Nadeem S, Ul Haq R. Model-based analysis of micropolar nanofluid flow over a stretching surface," *Eur. Phys. J. Plus*. 2014; 129(8).